Ultrathin 2D type-II p-n heterojunctions $La_2Ti_2O_7/In_2S_3$ with efficient charge separations and photocatalytic hydrogen evolution under visible light illumination

Erbing Hua[a,b,1], Shu Jin[a,1], Xiaorong Wang[b], Shuang Ni[c,**], Gang Liu[d,**], Xiaoxiang Xu[a,b,*]

[a] Clinical and Central Lab, Putuo People's Hospital, Tongji University, 1291 Jiangning Road, Shanghai, 200060, China
[b] Shanghai Key Lab of Chemical Assessment and Sustainability, School of Chemical Science and Engineering, Tongji University, 1239 Siping Road, Shanghai, 200092, China
[c] Science and Technology on Plasma Physics Laboratory, Laser Fusion Research Center, China Academy of Engineering Physics, Mianyang, 621900, China
[d] Shenyang National laboratory for Materials Science, Institute of Metal Research, Chinese Academy of Science, 72 Wenhua Road, Shenyang, 110016, China

ARTICLE INFO

ABSTRACT

In this work, novel 2D type-II p-n heterojunctions $La_2Ti_2O_7/In_2S_3$ have been fabricated. The heterojunctions exhibit much improved photocatalytic activity over individual moieties and their physical mixtures in which 18-fold increment in hydrogen production has been achieved under visible light illumination ($\lambda \geq 400$ nm). Their superior activities stem from intimate face-to-face contact between $La_2Ti_2O_7$ and In_2S_3 in the heterojunctions which guarantee facile charge interchange. Photoelectrochemical analysis suggests that efficient charge separations occur at the interfaces of the heterojunctions and contributes to a prolonged charge lifetime as well as the much enhanced photocatalytic activities. Such a simple strategy by fabricating ultrathin type-II p-n heterojunctions also warrant promising applications in other areas such as optoelectronics, sensors etc. whereby efficient charge separations are needed.

1. Introduction

Semiconductor photocatalysis has been considered as a promising technology for environment purification and solar energy conversions. The production of clean chemical fuel hydrogen (H_2) by photocatalytic processes is of great significance to cope with energy crisis and environmental problems [1–14]. This is simply because solar energy is vast and inexhaustible and is widely accessible all over the world whilst hydrogen is a clean energy resource whose recycling has minimal impact to the environment [15–20]. The practical deployment of this intriguing technique offers us a good opportunity to ultimately decarbonize our fossil-fuel based economy but still awaits significant breakthrough on photocatalytic materials. This has been realized that most photocatalysts investigated previously suffered from low solar to hydrogen efficiency (STH), primarily due to the occurrence of fast charge recombination events inside these materials that significantly outweigh the slow charge transfer kinetics at the interfaces [21–25]. For photocatalytic processes, separation of photo-generated charges is of crucial importance in determining the practical performance of a

semiconductor photocatalyst. How to promote the dissociation of photo-generated charges so as to be comparable with interfacial charge transfer kinetics remains a real challenge [26,27]. Semiconductor heterojunctions, in this regard, stand out as promising devices in dissociating photo-generated electron-hole pairs. Previous studies on semiconductor heterojunctions have witnessed a number of successes in generating long-lived charges, primarily due to the spatial separation of electrons and holes at the hetero-interfaces that reduce the risks of charge recombination. In particular, type II p-n heterojunctions are most suitable for this purpose. In this case, photo-generated electrons can be injected into n-type semiconductors while photo-generated holes tend to remain at or be pumped into the p-type semiconductors. Therefore, electrons and holes are prevented from contacting due to internally built electric field across the hetero-interfaces. Different kinds of type II p-n heterojunctions, such as BP/g-C_3N_4 [28,29], NiO/$Ca_2Nb_3O_{10}$ [30], MoS_2/R-GO/CdS [31], NiS/CdS [32], CdS/MoS_2 [33,34], $MoTe_2/MoS_2$ [35], TiO_2/NiO [36], p-TiO_2/n-TiO_2 [37], CdS/Cu_2O [38], $BiOBr/TiO_2$ [39], aza-CMP/C_2N [40] have been fabricated which demonstrate encouraging performance in photocatalysis. For

heterojunctions, connections between individual moieties are of critical importance as they determine the pathways for charge transportations. Compared to conventional type-II heterojunctions, ultrathin 2D type-II p-n heterojunctions own a number of useful features: (i) semiconductors contact in a face-to-face manner, offering the most charge transportation pathways; (ii) the ultrathin character of semiconductors ensure a very short migration distance for photo-generated charges; (iii) the large surface of individual semiconductor offers more reaction sites and allows further decorations.

Herein, we successfully fabricated ultrathin 2D type-II p-n heterojunctions $La_2Ti_2O_7/In_2S_3$ via a facile self-assembling method. The strong coulomb static force between $La_2Ti_2O_7$ and In_2S_3 due to their inverse Zeta potentials guarantees intimate contact of these two compounds which forms a firm basis for charge interchange. $La_2Ti_2O_7$ is a robust n-type semiconductor for water splitting under UV light illumination whist In_2S_3 is p-type semiconductor for visible light photocatalysis whose band edge positions match with $La_2Ti_2O_7$ for type-II heterojunctions. The so-formed heterojunctions demonstrates superior photocatalytic activity for hydrogen production from water under visible light illumination. Further photoelectrochemical (PEC) analysis suggests that such a special architecture plays a crucial role in separating photo-generated charges.

2. Experimental

2.1. Preparation of La₂Ti₂O₇ nanosheets

$La_2Ti_2O_7$ nanosheets were synthesized by a hydrothermal method according to the previous literature [41]. In a typical synthesis, 4 mmol $La(NO)_3 \cdot xH_2O$ (Aladdin, 99%) and 4 mmol $Ti(SO_4)_2$ (Aladdin, 99.99%) were dispersed into 20 mL distilled water to form homogeneous solution. Subsequently, 40 mL 2 M NaOH was added dropwisely into above solution under magnetic stirring. The so-formed suspensions were magnetically stirred for 4 h before transferred into a Teflon-lined autoclave for hydrothermal reactions. Typical reaction conditions are 230 °C for 24 h. The resultant powders were washed using distilled water until pH value approached 7. The powders were then filtered and dried at 80 °C for 12 h. Then the powder was treated with ultra-sonication in DMF for 48 h, dried at room temperature in vacuum oven for 12 h and labelled as LTO.

2.2. Preparation of In₂S₃ nanosheets

In_2S_3 nanosheets with lamellar morphologies were synthesized by a reflux method [42]. Typically, 1.5280 g $In(NO_3)_3 \cdot 4H_2O$, 1.4580 g hexadecyl trimethyl ammonium bromide (CTAB) and 0.9020 g thioacetamide (TAA) were dispersed in a round-bottom flask. 100 mL deionized water was added to the flask subsequently. The suspension was magnetically stirred for 10 min, heated slowly to 95 °C and refluxed at this temperature for 90 min. The resulting yellow powders were washed using distilled water and ethanol several times and dried at 80 °C for 12 h in a vacuum oven. Then the powders were sonicated in DMF for 48 h, and dried at room temperature in vacuum oven for 12 h. The resultant powders were labelled as IS. DMF serves as a good dispersant for both nanosheets and as it is an aprotic solvent, it helps to maintain surface charge of both nanosheets.

2.3. Fabrication of La₂Ti₂O₇/In₂S₃ nanosheets heterojunctions

The $La_2Ti_2O_7/In_2S_3$ nanosheets heterojunctions were fabricated by self-assembling processes driven by coulombic force between individual components. A schematic illustration of the fabrication process is displayed in Scheme 1. In a typical fabrication process, $La_2Ti_2O_7$ nanosheets and In_2S_3 nanosheets were ultra-sonicated separately in 10 mL dimethyformamide (DMF) till stable suspensions were formed. These two suspensions were then slowly mixed under sonication conditions.

Self-assembling processes can be envisaged as precipitations immediately appeared even under continuous sonication. The precipitants were filtered, dried at 80 °C for 12 h in vacuum oven and calcined at 180 °C in air for 2 h to strengthen mutual contact between $La_2Ti_2O_7$ and In_2S_3. The relative content of In_2S_3 within the heterojunctions was varied by controlling the initial mass ratios of $La_2Ti_2O_7/In_2S_3$ before self-assembling processes. A series of $La_2Ti_2O_7/In_2S_3$ mass ratios 2.5:1.0, 5.0:1.0, 7.5:1.0, 10.0:1.0 and 12.5:1.0 were investigated and were denoted by these numbers.

2.4. Materials characterizations

Phase purity and compositions were examined by X-ray powder diffraction (XRD) techniques (Bruker D8 Focus diffractometer). The incident radiation was Cu $K_{\alpha 1}$ ($\lambda = 1.5406$ Å) and Cu $K_{\alpha 2}$ ($\lambda = 1.5444$ Å). The step size for data collection was 0.01° with a collection time of 10 s at each step. Microstructures were examined on a field emission scanning electron microscope (Hitachi S4800) equipped with a Mica energy dispersive X-ray spectroscopy (EDS) analysis system and a transmission electron microscope (JEOL JEM-2100). Diffuse reflectance spectra were collected on a UV–vis spectrophotometer (JASCO-750) and analyzed using the JASCO software suite. $BaSO_4$ was used as a reference non-absorbing material. Specific surface areas were analyzed on a Micromeritics instrument TriStar 3000 and were calculated via the Brunauer-Emmett-Teller (BET) model. FT-IR data was collected and analyzed on Thermal scientific NICOLET IS10. Surface chemical compositions and binding energy of constituent elements were analyzed using X-ray photoelectron spectroscopy (Thermo Escalab 250 with a monochromatic Al Ka X-ray source). All binding energies were referred to the adventitious carbon C 1*s* peak at 284.7 eV. Raman spectra were measured at room temperature on a self-assembled UV Raman spectrograph (Renishaw inVia) with the spectral resolution of 1 cm $^{-1}$. 325 nm of the He-Cd laser with an output of 20 mW was used as the exciting source.

2.5. Photocatalytic activity

Photocatalytic activity of as-prepared samples was evaluated by monitoring their hydrogen production from water under visible light illumination ($\lambda \geq 400$ nm). A top-irradiation-type reactor connected to a gas-closed circulation and evacuation system (Perfect Light, Labsolar-IIIAG) was used to perform the experiment. In a typical experiment, 60 mg sample powders were dispersed in 100 ml 0.05 M Na_2S/Na_2SO_3 aqueous solution, which was sealed in the reactor. Evacuation was performed first to the reactor for 30 min in order to remove air dissolved in the solution. Platinum was used as a co-catalyst to promote photo-reduction reactions and was loaded onto the samples by a photo-deposition method: H_2PtCl_6 aqueous solution was added dropwisely into the reactor and was reduced into Pt nanoparticles by irradiating the solution ($\lambda \geq 400$ nm) [43]. The amounts of Pt loading was 2 wt%. A 300 W Xenon lamp (Perfect Light, PLX-SXE300) was used as a light source. A UV cut-off filter ($\lambda \geq 400$ nm) was applied to generate visible light irradiation. The gas component within the reactor was then analyzed using an online gas chromatograph (TECHCOMP, GC7900) with a TCD detector. Water jacket was used to stabilize the temperature of reactor around 20 °C. Magnetic stirring was applied to the solution during the entire experiment.

2.6. Preparation of photoelectrodes and photoelectrochemical measurements

The photo-electrodes were prepared by a drop-casting method [44]. In a typical fabrication process, 6.0 mg of the sample powders were dispersed into 6 mL ethanol by sonication to form a suspension. The suspension was dropped onto fluorine-doped tin oxide glass slides (FTO, 1 × 3 cm) and was dried in air. The deposited glass was calcined
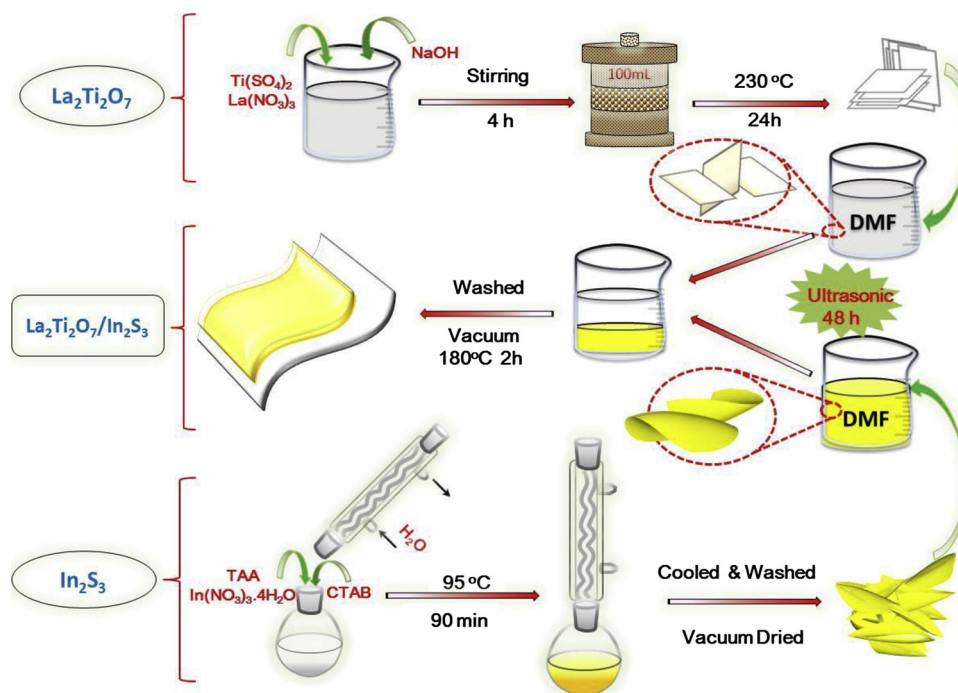
Scheme 1. Schematic illustration of the proposed synthetic route for the fabrication of ultrathin 2D type-II p-n heterojunctions La$_2$Ti$_2$O$_7$/In$_2$S$_3$.

at 180 °C for 2 h to strengthen particle contact. Photo-electrochemical (PEC) measurements were performed in a three-electrode configuration using a Zahner electrochemical workstation. The as-prepared photo-electrode, Pt foil (10 × 10 mm) and the Ag/AgCl electrode were used as the working, counter and reference electrodes, respectively. 0.1 M K$_3$PO$_4$/K$_2$HPO$_4$ aqueous solution was employed as the electrolyte and a buffer (pH = 7.95). A 300 W Xenon lamp (Perfect Light, PLX-SXE300) was used as a light source. Incident light was controlled by an electronic timer and shutter (DAHENG, GCI-73). Impedance analysis was performed from 0.1 MHz to 0.1 Hz with 10 mV amplitude.

3. Results and discussions

3.1. Phase purity and compositions

X-ray powder diffraction patterns of all samples are illustrated in Fig. 1. Standard patterns of In$_2$S$_3$ (JCPDS 00-025-0390) and La$_2$Ti$_2$O$_7$ (ICSD 5416) are also included for comparisons [44,45]. For pristine In$_2$S$_3$, peaks at 27.4°, 33.5° and 47.7° are ascribed to the (109), (220) and (22 12) reflections respectively. The much broad peak at 33.5° with respect to others suggests anisotropic growth of In$_2$S$_3$ particles. The ratio between (22 12)/(109) reflection is much larger than that in the standard pattern, implying that these particles grow preferentially along (22 12) plane [46,47]. This can be rationalized by the presence of cationic surfactant CTAB during synthesis which may tend to adsorb on planes full of S^{2-}, e.g. (220) planes, preventing further growth of those planes [42]. Similar phenomenon can be realized in as-prepared La$_2$Ti$_2$O$_7$ in which (012) reflection at 21.1° is poorly resolved with respect to remaining ones, suggesting anisotropic growth of sample particles. (012) planes of La$_2$Ti$_2$O$_7$ containing a high level of La^{3+} ions which tends to bind with OH- anions in the solution, resulting in a poor growth of those planes. Combining La$_2$Ti$_2$O$_7$ and In$_2$S$_3$ does not lead to discernable changes on diffraction peaks, indicating that crystal integrity of both components is maintained.

3.2. Microstructures

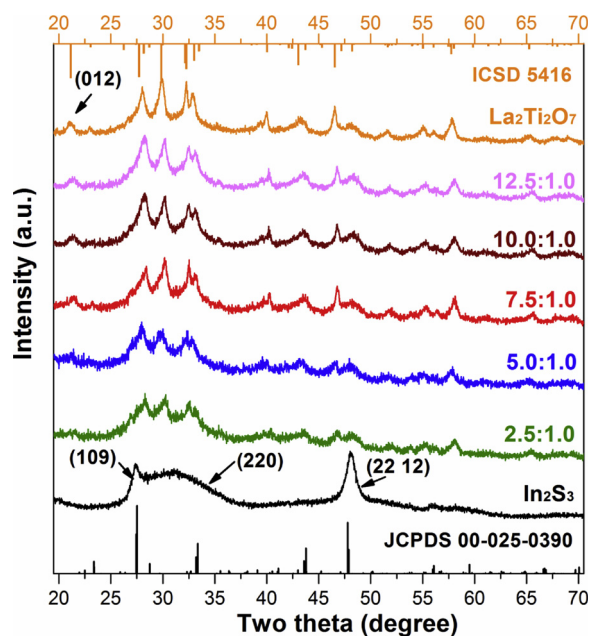Morphologies of sample particles were further inspected under

Fig. 1. XRD patterns of In$_2$S$_3$, La$_2$Ti$_2$O$_7$ and the La$_2$Ti$_2$O$_7$/In$_2$S$_3$ nanosheets heterojunctions with different mass ratios between La$_2$Ti$_2$O$_7$ and In$_2$S$_3$. Pristine In$_2$S$_3$ and La$_2$Ti$_2$O$_7$ are shown for comparisons. Standard XRD patterns for In$_2$S$_3$ and La$_2$Ti$_2$O$_7$ are also included.

microscopy conditions. Typical SEM images of In$_2$S$_3$, La$_2$Ti$_2$O$_7$ and the La$_2$Ti$_2$O$_7$/In$_2$S$_3$ nanosheets heterojunctions with different mass ratios are displayed in Fig. 2. Both In$_2$S$_3$ and La$_2$Ti$_2$O$_7$ display nanosheet-like morphologies, being in conformity with expectations from XRD analysis. The differences of their particles lie in the size of the nanosheets. In$_2$S$_3$ is composed of nanosheets with lateral dimension around 200 nm and thickness around a few nanometers (Fig. 2a, Figure S1b, c). La$_2$Ti$_2$O$_7$ however, has much large nanosheets with lateral dimension more than 500 nm but with a similar thickness less than 10 nm with regard to In$_2$S$_3$ (Fig. 2g, Figure S1a). Thereby, combining these two
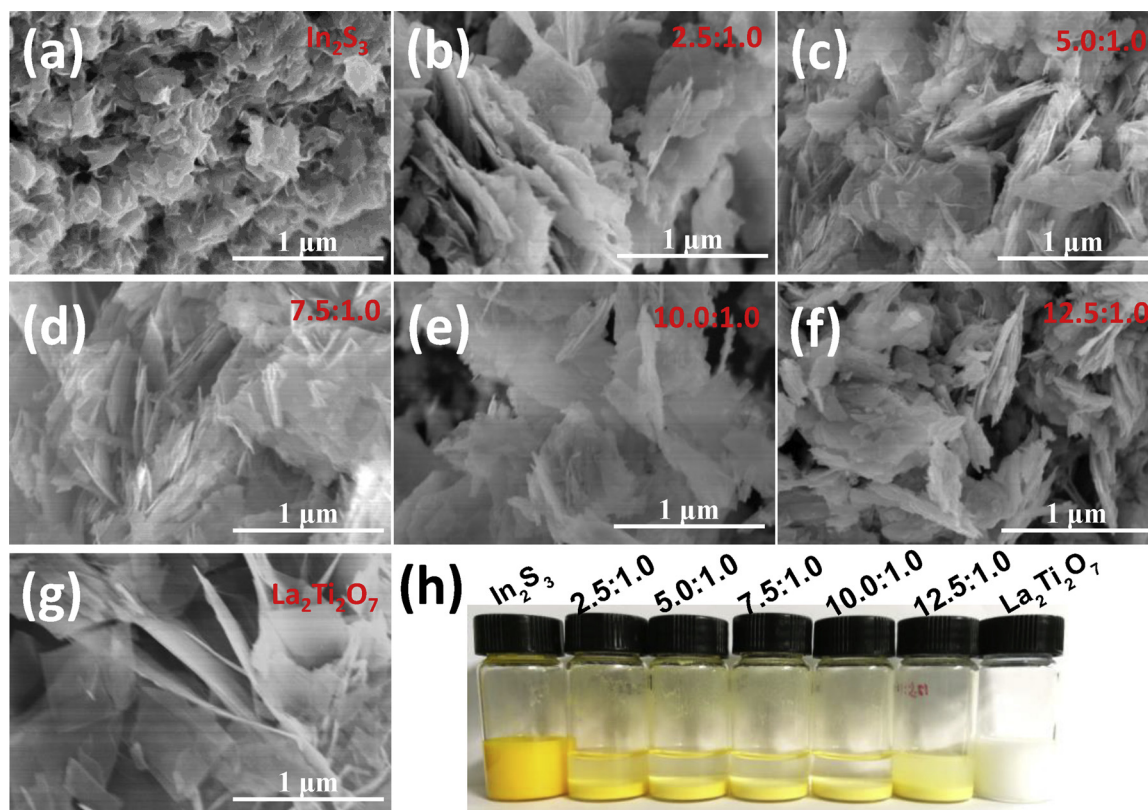
Fig. 2. Typical SEM images of In_2S_3 (a), $La_2Ti_2O_7/In_2S_3$ nanosheet heterojunctions with different mass ratio of $La_2Ti_2O_7/In_2S_3$: 2.5:1.0 (b), 5.0:1.0 (c), 7.5:1.0 (d), 10.51.0 (e), 12.5:1.0 (f); $La_2Ti_2O_7$ (g), and digital photos of above samples in DMF (h).

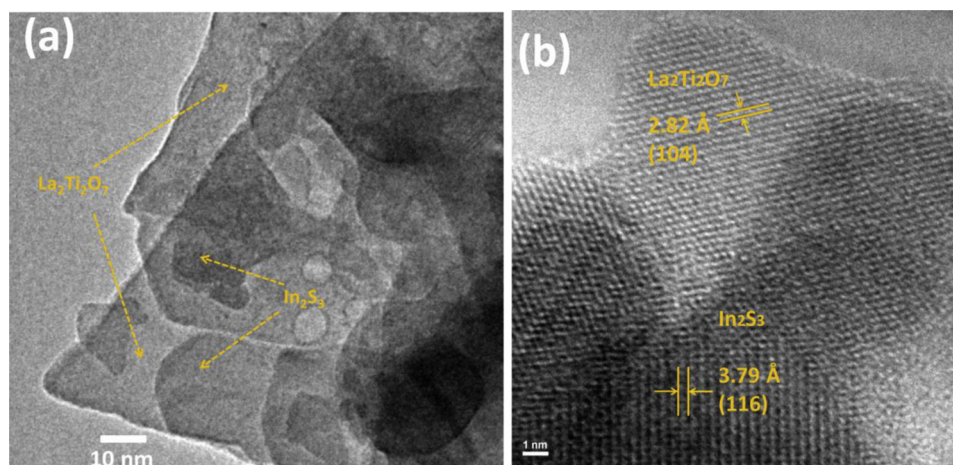**Fig. 3.** Typical transmission electron microscope (TEM) images of $La_2Ti_2O_7/In_2S_3$ nanosheet heterojunctions (mass ratio 7.5:1.0) (a) and High Resolution TEM (HRTEM) image of $La_2Ti_2O_7/In_2S_3$ nanosheet heterojunctions (mass ratio of 7.5:1.0) (b).

types of nanosheets will lead to a face-to-face contact between individual particles as long as there are strong interactions between them. This is indeed the case here that compact nanosheet assemblies can be formed across various $La_2Ti_2O_7/In_2S_3$ mass ratios (Fig. 2b–f). Relatively small In_2S_3 nanosheets can be identified on larger $La_2Ti_2O_7$ nanosheets according to high resolution TEM inspections and EDX mapping analysis (Fig. 3 and Figure S3). The strong interactions between In_2S_3 and $La_2Ti_2O_7$ can be envisaged before and after mixing In_2S_3 and $La_2Ti_2O_7$ DMF suspensions. Stable In_2S_3 and $La_2Ti_2O_7$ suspensions are immediately precipitated upon mixing (Fig. 2h). The so-formed precipitants are quite robust as they are retained even under long term sonication. Such phenomenon can be well explained by the strong columbic attracting force between individual In_2S_3 and $La_2Ti_2O_7$

nanosheet. In_2S_3 nanosheets have a -0.13 V (vs NHE) Zeta potential in DMF while $La_2Ti_2O_7$ nanosheets own a + 0.33 V (Figure S4). Thereby, strong binding occurs between In_2S_3 and $La_2Ti_2O_7$ nanosheets in a face-to-face manner. Such unique heterostructures are highly beneficial for charge interchange between In_2S_3 and $La_2Ti_2O_7$ as interfacial resistance is minimized. This apparently outweighs conventional heterostructures whereby only point-to-point contact exists among particles [43,46,48,49].

3.3. FT-IR and Raman spectra

To get a deeper insight into the so-formed $La_2Ti_2O_7/In_2S_3$ nanosheets heterojunctions, we have performed FT-IR and Raman
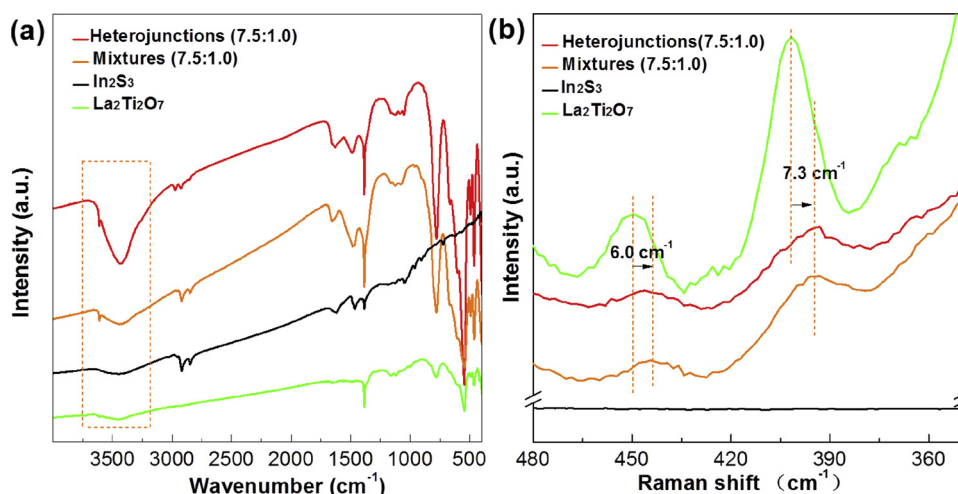
Fig. 4. FT-IR (a) and Raman spectra (b) of the as-prepared samples.

spectroscopy analysis on as-prepared sample powders. The results are illustrated in Fig. 4 in which $La_2Ti_2O_7/In_2S_3$ nanosheets heterojunctions, physical mixtures of $La_2Ti_2O_7/In_2S_3$ nanosheets, pristine $La_2Ti_2O_7$ and In_2S_3 are compiled for comparisons. For IR spectra, various vibration peaks of pristine $La_2Ti_2O_7$ and In_2S_3 are all retained in heterojunctions as well as in physical mixtures of $La_2Ti_2O_7/In_2S_3$. However, there are apparent differences on the intensity of broad peaks around $3300\,cm^{-1}$. These peaks normally assigned to OH stretching mode of water adhered to the surface of sample powders and are found to be strongest in $La_2Ti_2O_7/In_2S_3$ nanosheets heterojunctions. Such an increase in the hydrophilicity after fabrication of heterojunctions indicates a substantial enhancement in the polarity of individual component, which in turn, reflects the strong interactions between $La_2Ti_2O_7$ and In_2S_3. This can be rationalized by the strong electric field at the interface of the heterojunctions due to large Zeta potential differences between $La_2Ti_2O_7$ and In_2S_3 as well as the tiny thickness of the heterojunctions (a few nanometers). On the other hand, Raman spectra provide a more direct evidence for the strong interactions between $La_2Ti_2O_7$ and In_2S_3 in the heterojunctions. Peaks at $405\,cm^{-1}$ and $448\,cm^{-1}$ are ascribed to La-O and Ti-O vibration mode in $La_2Ti_2O_7$ [50–52]. These peaks are substantially broadened in heterojunctions and physical mixtures of $La_2Ti_2O_7$ and In_2S_3, implying a reduced polarizability of $La_2Ti_2O_7$ with respect to pristine one [53]. This can be attributed to the strong electric field at the interface of heterojunctions that considerably distorts the electron cloud of $La_2Ti_2O_7$. More importantly, there are substantial negative shifts of these two peaks in heterojunctions, which probably stems from the strong linkage between $La_2Ti_2O_7$ and In_2S_3 that weakens the bond strengthen of La-O and Ti-O, resulting in a smaller Raman shift of these two vibration modes.

3.4. XPS characterization

The surface nature of these samples is further inspected by XPS techniques. Pristine In_2S_3 displays two strong peaks at 444.8 and 452.3 eV, assignable to In $3d_{5/2}$ and In $3d_{3/2}$ state [44,54–56]. These two peaks are found to be shifted to a lower binding energy in the heterojunctions and physical mixtures of $La_2Ti_2O_7/In_2S_3$ (Fig. 5a and b). Recalling the fact that In_2S_3 is a p-type semiconductor whose Fermi level is ought to be lower than n-type semiconductor $La_2Ti_2O_7$. Such a decrease in the binding energy of indium likely originates from electron transfers from $La_2Ti_2O_7$ to In_2S_3. This is further confirmed by similar phenomenon of S 2p state in which peaks corresponding to S $2p_{3/2}$ and S $2p_{1/2}$ at 161.3 and 162.5 eV all shift to a lower binding energy [38,42]. Nevertheless, binding energies of Ti 2p and O 1s state in $La_2Ti_2O_7$ are not severely altered (Fig. 5c and d). This is probably due to

strong electric field at the interface of $La_2Ti_2O_7$ and In_2S_3 which pulls electron cloud of In_2S_3 towards $La_2Ti_2O_7$, counterbalancing the electron loss in $La_2Ti_2O_7$.

3.5. UV–vis spectra and band edge positions

The optical properties of pristine In_2S_3 $La_2Ti_2O_7$ nanosheets and $La_2Ti_2O_7/In_2S_3$ heterojunctions at various mass ratios of $La_2Ti_2O_7/In_2S_3$ were studied by UV–vis diffuse reflectance spectroscopy. As shown in Fig. 6a, $La_2Ti_2O_7$ is a wide band gap semiconductor with absorption edge lies approximately at 325 nm. In contrast, In_2S_3 is a small band gap semiconductor whose absorption edge approaches as far as 600 nm. Constructing heterojunctions, however, has little impact on the position of absorption edges. Instead, it changes the intensity of visible light absorption according to different mass ratios of $La_2Ti_2O_7/In_2S_3$. Thereby, optical properties of $La_2Ti_2O_7$ and In_2S_3 in the heterojunctions are similar to pristine ones and the level of light absorption can be tuned simply by varying the mass ratios of $La_2Ti_2O_7/In_2S_3$ in the heterojunctions. XPS valence band scan was then introduced to examine the band edge positions of all samples. Fig. 6b illustrates the XPS valence band scan for pristine $La_2Ti_2O_7$, In_2S_3 and $La_2Ti_2O_7/In_2S_3$ heterojunctions (mass ratio 7.5: 1.0). Pristine $La_2Ti_2O_7$ owns a valence band edge at approximately 3.26 eV whist for In_2S_3, this value moves to 0.88 eV. On the other hand, the flat-band potential (i.e. Fermi level) determined by extrapolating the linear part of Mott-Schottky curves down to the potential axis read $-0.60\,V$ (vs. NHE) and $-0.38\,V$ (vs. NHE) for $La_2Ti_2O_7$ and In_2S_3 respectively (Fig. S8). Considering the band gap values of these two compounds, their band edge positions can be tentatively determined. Fig. 6c schematically illustrates the band edge positions for both $La_2Ti_2O_7$ and In_2S_3. In_2S_3 has a conduction band edge 0.57 V more negative than $La_2Ti_2O_7$ while $La_2Ti_2O_7$ owns a valence band edge 2.16 eV more positive than In_2S_3. Thereby, type-II p-n heterojunctions can be formed between $La_2Ti_2O_7$ and In_2S_3.

3.6. Photocatalytic activity

The photocatalytic activity of all samples was evaluated by monitoring the hydrogen evolution in the presence of a sacrificial reagent under visible light illumination ($\lambda \geq 400\,nm$). 0.05 M Na_2S-Na_2SO_3 aqueous solutions were used as the sacrificial reagent to promote photocatalytic reduction reactions. For direct comparisons, experimental parameters such as co-catalyst loading, temperature, amounts of the sacrificial reagent etc., were all kept the same for all samples. The temporal hydrogen production of all samples is displayed in Fig. 7a. All samples containing In_2S_3 demonstrate continuous hydrogen evolution
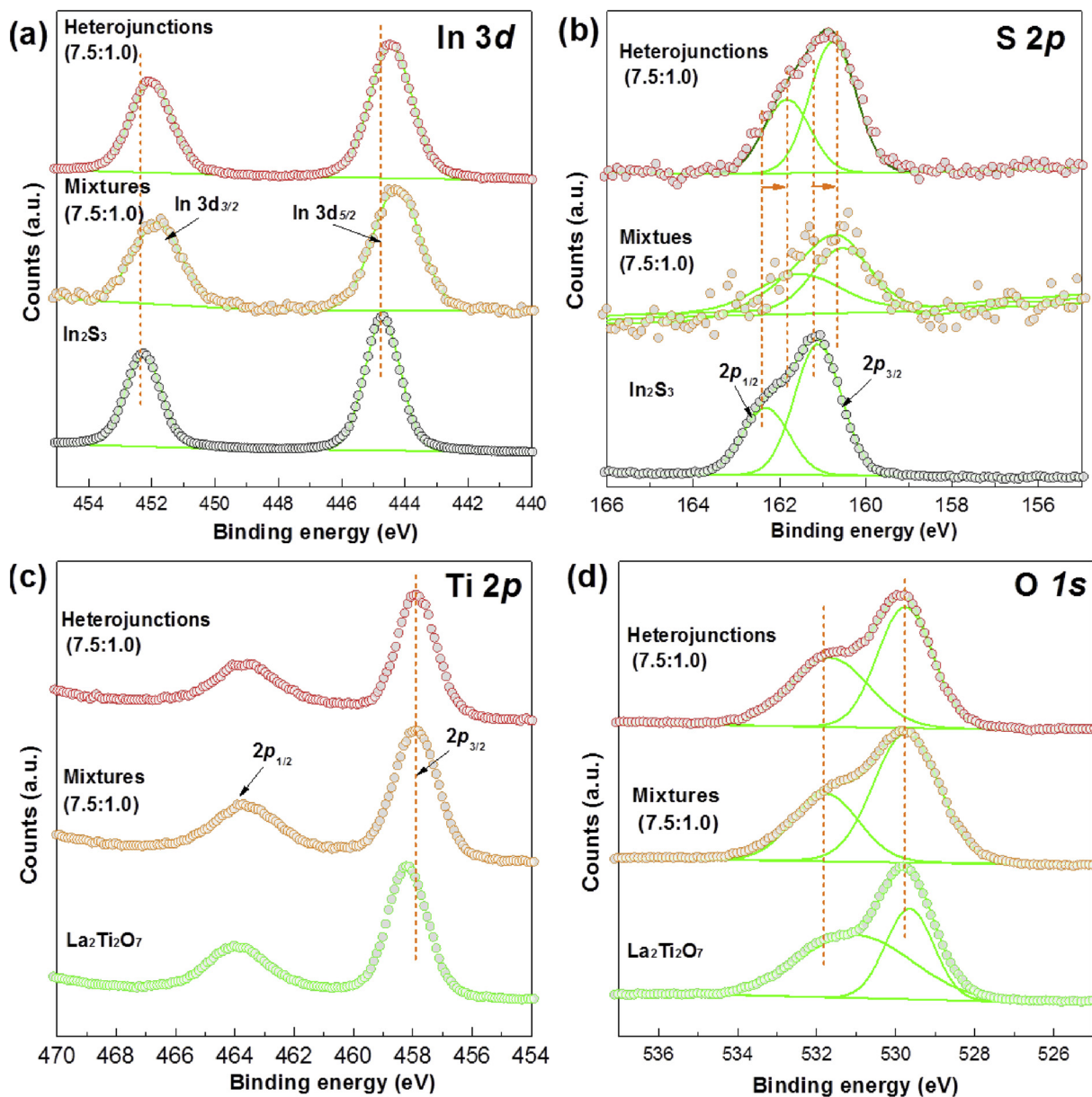
Fig. 5. XPS spectra of freshly prepared samples: (a) In 3d; (b) S 2p; (c) Ti 2p ; (d) O 1 s.
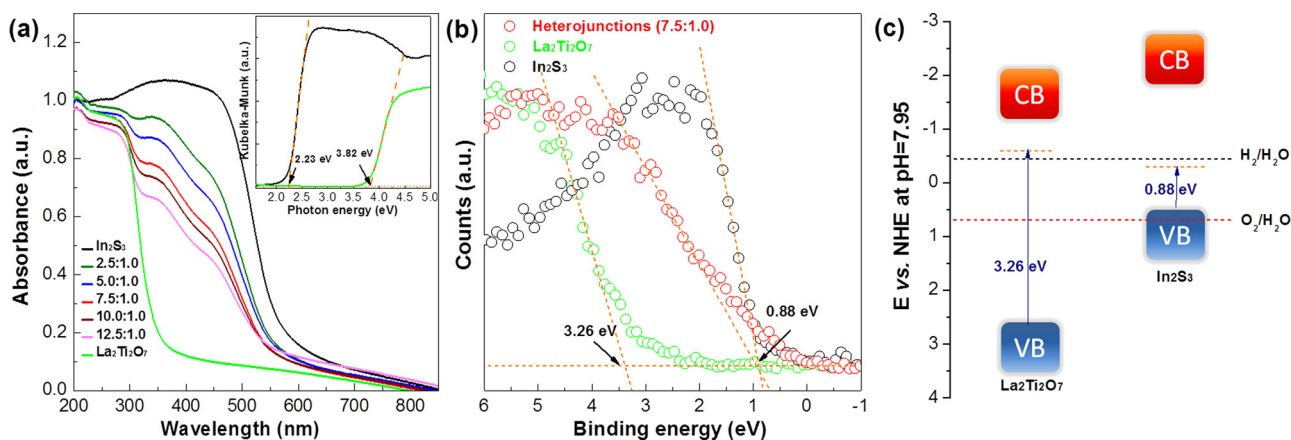

Fig. 6. (a): UV–vis diffuse reflectance spectra of In_2S_3, $La_2Ti_2O_7$ and the $La_2Ti_2O_7/In_2S_3$ nanocomposites with different mass ratios and Kubelka–Munk transformation of absorption curves of $La_2Ti_2O_7$ and In_2S_3; (b): XPS valence band scan for $La_2Ti_2O_7$, In_2S_3 and $La_2Ti_2O_7/In_2S_3$ heterojunctions (mass ratio 7.5: 1.0); (c): schematic illustration of the band edge positions for both $La_2Ti_2O_7$ and In_2S_3.

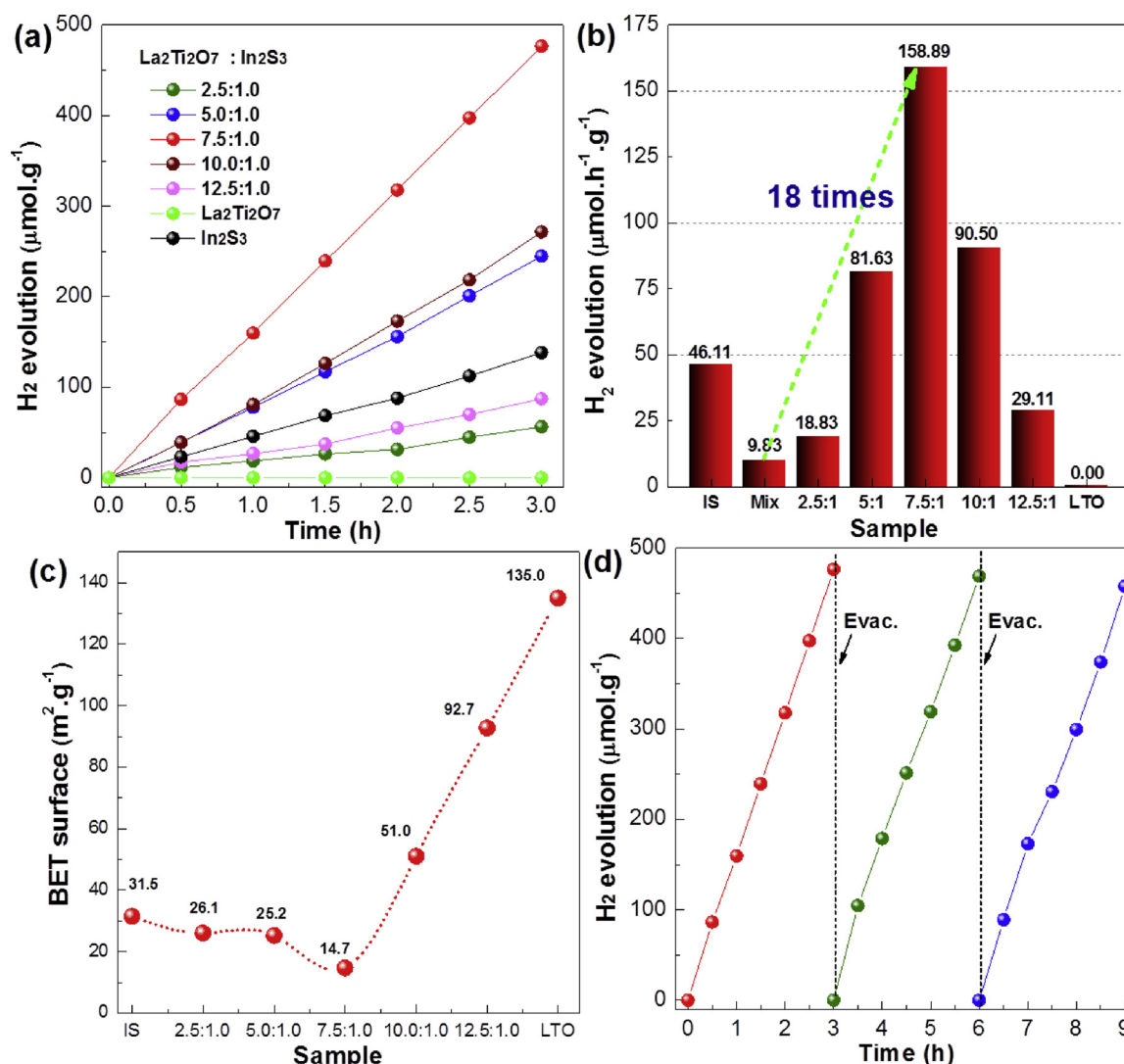**Fig. 7.** (a) Temporal hydrogen evolution for the La$_2$Ti$_2$O$_7$/In$_2$S$_3$ heterojunctions fabricated with different mass ratios of La$_2$Ti$_2$O$_7$ to In$_2$S$_3$ (2.5:1.0, 5.0:1.0, 7.5:1.0, 10.0:1.0 and 12.5:1.0) under visible light illumination ($\lambda \geq 400$ nm), pristine In$_2$S$_3$ and La$_2$Ti$_2$O$_7$ are also included for comparisons; (b) average hydrogen production rate for different samples, "Mix" denotes physical mixtures of La$_2$Ti$_2$O$_7$ and In$_2$S$_3$ (mass ratio 7.5:1.0), "LTO" denotes for La$_2$Ti$_2$O$_7$; (c) BET surface area of samples with different mass ratio of La$_2$Ti$_2$O$_7$ to In$_2$S$_3$; (d) repeated courses of H$_2$ evolution for 9 h with intermittent evacuation at every 3 h for La$_2$Ti$_2$O$_7$/In$_2$S$_3$ nanosheets heterojunctions (mass ratio 7.5:1.0).

for the whole illumination period, suggesting that they are active photocatalysts for water reduction reactions. This is in contrast to pristine La$_2$Ti$_2$O$_7$ which remains inactive for the whole experimental period, being consistent with its wide band gap semiconductivity. Therefore, In$_2$S$_3$ is indispensable for visible light photocatalytic performance. Interestingly, heterojunctions with La$_2$Ti$_2$O$_7$/In$_2$S$_3$ mass ratio 5.0:1.0, 7.5:1.0 and 10.0:1.0 display a much higher photocatalytic activity than pristine In$_2$S$_3$ even though the amounts of In$_2$S$_3$ in these heterojunctions are significantly reduced (Fig. 7a). Further analysis on the average hydrogen production rate reveals an optimal mass ratio at 7.5:1.0 for La$_2$Ti$_2$O$_7$/In$_2$S$_3$ nanosheet heterojunctions. Heterojunctions at this mass ratios demonstrate an average hydrogen production rate almost 3.5 times higher than pristine In$_2$S$_3$ and 18 times higher than physical mixtures of La$_2$Ti$_2$O$_7$ and In$_2$S$_3$ (Fig. 7b and Figure S5b). Such a strikingly improvement cannot be ascribed to a simply increase in the reactive sites as surface area is decreased after fabricating La$_2$Ti$_2$O$_7$/In$_2$S$_3$ nanosheet heterojunctions, being minimized at mass ratio 7.5:1.0 (Fig. 7c). Furthermore, prolonged experiments suggest that heterojunctions are stable for repeated cycles where no apparent degradation on photocatalytic activity is seen.

3.7. Photoelectrochemical measurements

To better understand the superior photocatalytic activity of La$_2$Ti$_2$O$_7$/In$_2$S$_3$ nanosheets heterojunctions, photoelectrochemical measurements based on photo-electrodes deposited with sample powders were performed. Fig. 8a illustrates the current-voltage curves for La$_2$Ti$_2$O$_7$/In$_2$S$_3$ heterojunctions (mass ratio 7.5:1.0) under chopped light illumination. Data for pristine In$_2$S$_3$ was also included for comparisons. As a typical character of p-type semiconductor, In$_2$S$_3$ displays clear cathodic photocurrent under visible light illuminations with onset potential lies approximately around 0.3 V (vs NHE). La$_2$Ti$_2$O$_7$/In$_2$S$_3$ heterojunctions (mass ratio 7.5:1.0), however, show both cathodic and anodic photocurrent under visible light illuminations. Recalling the fact that La$_2$Ti$_2$O$_7$ is n-type wide band gap semiconductor and is not active under visible light illuminations, the appearance of anodic photocurrent is clear evidence that photo-generated electrons in In$_2$S$_3$ can be transferred onto La$_2$Ti$_2$O$_7$, confirming the successful fabrication of type-II p-n heterojunctions. Besides, compared to physical mixtures of La$_2$Ti$_2$O$_7$/In$_2$S$_3$, heterojunctions own a much higher photocurrent, indicating that charge separations in heterojunctions occur more easily (Fig. 8b). This can be ascribed to the unique face-to-face contact
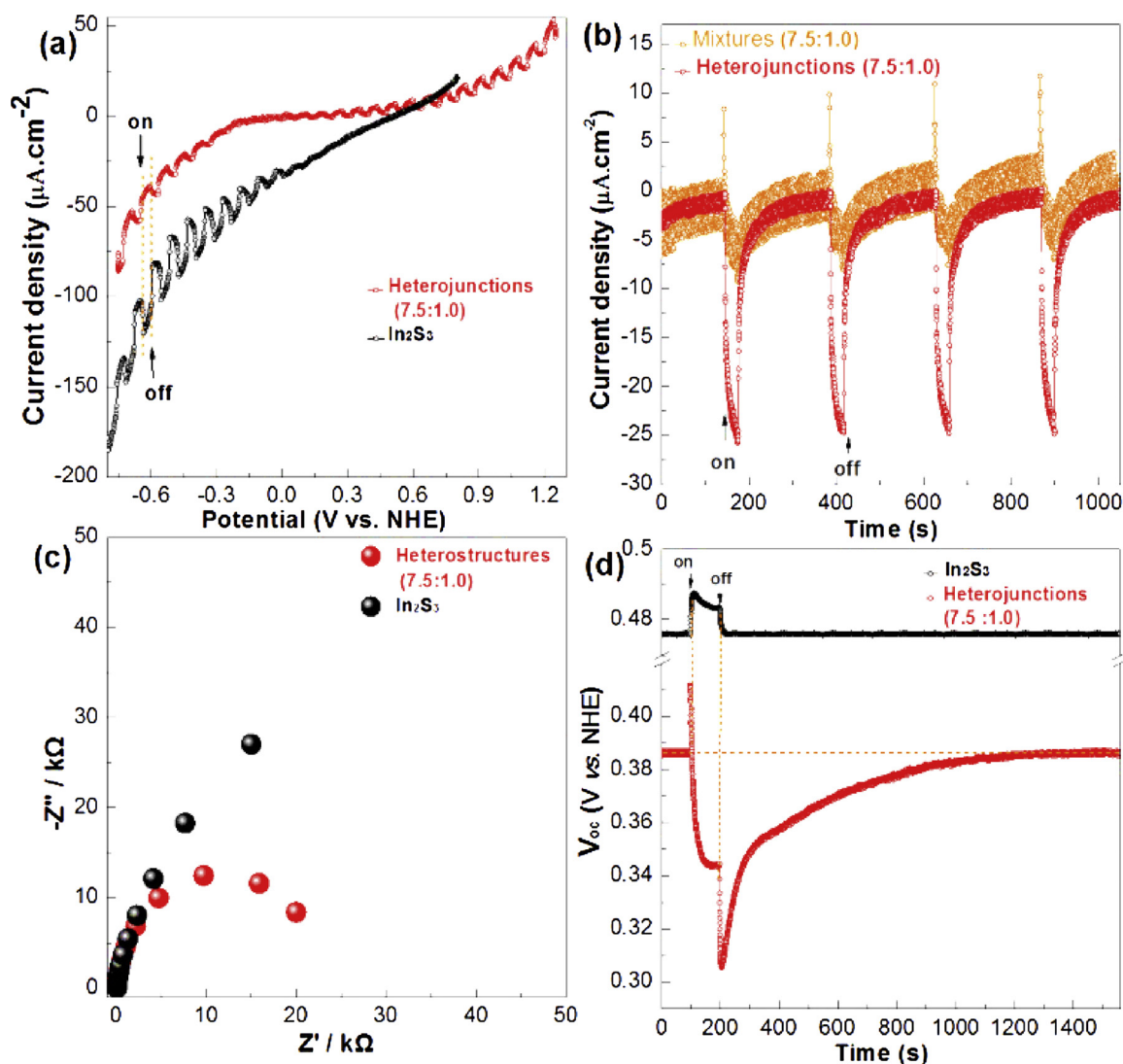
Fig. 8. (a) Current-voltage curves in aqueous 0.1 M K_3PO_4-K_2HPO_4 solution under chopped visible-light illumination ($\lambda \geq 400$ nm), Scanning rate: 20 mV/s; (b) Photocurrent versus time response of photoelectrodes at a bias of -0.4 V vs NHE under chopped light illumination (irradiation and dark time is 30 and 180 s, respectively) for $La_2Ti_2O_7$/In_2S_3 heterojunctions (mass ratio 7.5:1.0) and $La_2Ti_2O_7$/In_2S_3 physical mixtures (mass ratio 7.5:1.0); (c) V_{oc} time profile of In_2S_3, $La_2Ti_2O_7$/In_2S_3 heterojunctions (mass ratio 7.5:1.0) under visible light illumination; (d) Nyquist plot of impedance spectra for the same electrodes with electrical bias (V = 1.23 V vs NHE) under visible light illumination ($\lambda \geq 400$ nm).

between $La_2Ti_2O_7$ and In_2S_3 in the heterojunctions that allows efficient charge transportations. This is further supported by the much smaller interfacial charge transfer resistance for heterojunctions compared to physical mixtures of $La_2Ti_2O_7$/In_2S_3 (Fig. 8c).

To further study the charge separations in the heterojunctions, we have performed open-circuit voltage decay (OCVD) experiments on $La_2Ti_2O_7$/In_2S_3, nanosheets heterojunctions. Data for pristine In_2S_3 is also included for comparisons (Fig. 8c). The open-circuit voltage (V_{oc}) in the photoelectrochemical cell configuration represents the voltage difference between the Fermi levels of the semiconductor work electrode and the counter electrode. Illuminating n-type/p-type semiconductor induces a negative/positive shift of the Fermi level due to electron/hole accumulation in the semiconductor after consuming holes/electrons at the semiconductor/electrolyte interface. A steady V_{oc} will be reached once electron/hole accumulation competes with charge recombination or other electron consumption events. Likewise, decay of V_{oc} will start upon terminating the illumination and is governed by various electron dissipation pathways (e.g., charge recombination) [21].For pristine In_2S_3, V_{oc} time profile is characterized by a sudden increase and a prompt decay process upon light on and off,

corresponding to a rapid accumulation and dissipation of the photo-generated holes, being consistent with its p-type semiconductivity. There is also a clear attenuation trend before V_{oc} reaches a steady state during light illumination, indicating that hole accumulation is sequentially modulated by fast hole disposal procedures. The rapid restoration of V_{oc} back to its dark value upon light termination implies short hole lifetime in pristine In_2S_3. On the contrary, $La_2Ti_2O_7$/In_2S_3 nanosheets heterojunctions (7.5:1.0) shows distinct V_{oc} time profile which can be separated into several steps: first, the V_{oc} undergoes a sudden increase upon light illumination, corresponding to the accumulation of holes due to electron consumption at the semiconductor/electrolyte interface, being similar to pristine In_2S_3. However, this V_{oc} is dropped almost immediately to a value lower than the one in the dark, suggesting that electrons, instead of holes, start to accumulate in the heterojunctions. This can be explained by the nature of this type-II heterojunctions that $La_2Ti_2O_7$ strongly accepts photo-generated electrons from In_2S_3, resulting in a net storage of negative charge in the heterojunctions. During the extended light illumination period, V_{oc} keeps decreasing until a steady value is reached, corresponding to continuous collection of electrons in $La_2Ti_2O_7$ from In_2S_3 until this

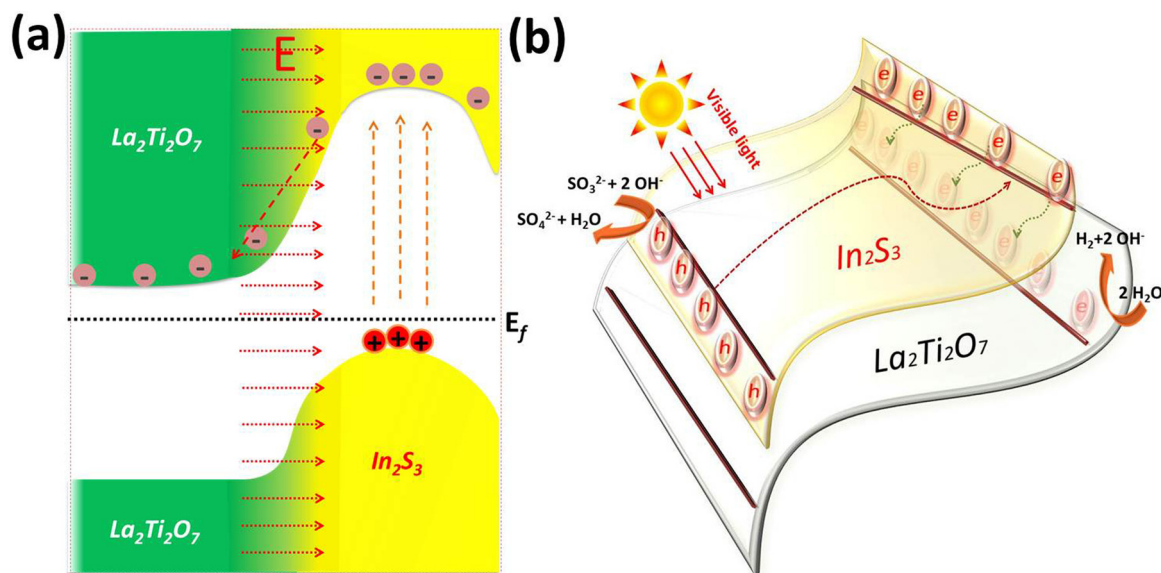**Fig. 9.** Proposed band structure model of La$_2$Ti$_2$O$_7$/In$_2$S$_3$ nanosheet heterojunctions (a); schematic representation of heterojunctions morphologies and photocatalytic reactions (b).

process is counterbalanced by various electron dissipation pathways. However, upon light termination, a further drop of V$_{oc}$ is observed, probably due to the elimination of holes stored in In$_2$S$_3$ that contributes to a net increase in the negative charge in the heterojunctions. In the final step, V$_{oc}$ slowly decays back to its dark value which takes almost 1000s, indicating extremely long lifetime of stored electrons in the heterojunctions. Therefore, by fabricating La$_2$Ti$_2$O$_7$/In$_2$S$_3$ nanosheets heterojunctions, photo-generated electrons and holes are separately efficient with a much prolonged lifetime, being responsible for the superior photocatalytic activity.

We can now tentatively explain the underlying mechanism of these nanosheet heterojunctions for photocatalytic reactions. A schematic illustration of their band structures and morphologies is shown in Fig. 9. Combining In$_2$S$_3$ and La$_2$Ti$_2$O$_7$ with different semiconductivity (p-type and n-type) results in an equalization of their Fermi levels which in turn, induces band bending and a strong electric field at their interface. Such a strong electric field is extremely helpful in separating photo-generated electron and holes. More specifically, photo-generated electrons in In$_2$S$_3$ are driven by the electric field onto La$_2$Ti$_2$O$_7$, which then participate in water reduction reactions. The unique face-to-face contact of In$_2$S$_3$ and La$_2$Ti$_2$O$_7$ nanosheets in the heterojunctions allows facile electron migrations from In$_2$S$_3$ to La$_2$Ti$_2$O$_7$, contributing the efficient charge separations and superior photocatalytic activity. This simple strategy by fabricating ultrathin 2D p-n heterojunctions can be well extended too other systems as long as strong interactions between individual moieties in the heterojunction can be established.

4. Conclusions

We have successfully fabricated 2D type-II p-n heterojunctions La$_2$Ti$_2$O$_7$/In$_2$S$_3$ via a simple self-assembling method. Microscopy analysis suggests that In$_2$S$_3$ and La$_2$Ti$_2$O$_7$ nanosheets in the heterojunction are aligned in a face-to-face manner. Spectroscopy analysis indicates there is strong interactions between In$_2$S$_3$ and La$_2$Ti$_2$O$_7$ nanosheets in the heterojunction that their hydrophilicity and bond vibration are somewhat changed. The so-formed La$_2$Ti$_2$O$_7$/In$_2$S$_3$ nanosheet heterojunctions demonstrate a much improvement photocatalytic activity for hydrogen production from water. An optimal mass ratio of La$_2$Ti$_2$O$_7$ to In$_2$S$_3$ was found at 7.5:1.0 which give an average hydrogen production rate almost 3.5 times higher than pristine In$_2$S$_3$ and 18 times higher than physical mixtures of La$_2$Ti$_2$O$_7$ and In$_2$S$_3$. This is likely originated

from the firm anchorage of In$_2$S$_3$ onto La$_2$Ti$_2$O$_7$ and a face-to-face intimate contact between these two semiconductors that allows rapid charge interchange. Further PEC analysis suggests that La$_2$Ti$_2$O$_7$ is capable of accepting electrons from In$_2$S$_3$ and lifetime of photo-generated electrons are significantly prolonged, being responsible for the superior photocatalytic activity. The facile method for the fabrication of 2D p-n La$_2$Ti$_2$O$_7$/In$_2$S$_3$ nanosheets heterojunctions as well as the strategy to construct type-II band alignment architectures may shed a light on the design and development of high efficient photocatalytic systems.

Appendix A. Supplementary data

Supplementary material related to this article can be found, in the online version, at doi:https://doi.org/10.1016/j.apcatb.2019.01.024.

References

[1] A. Fujishima, K. Honda, Nature 238 (1972) 37–38.
[2] J.S. Zhang, X.F. Chen, K. Takanabe, K. Maeda, K. Domen, J.D. Epping, X.Z. Fu, M. Antonietti, X.C. Wang, Angew. Chemie Int. Ed. English 49 (2010) 441–444.
[3] X.X. Xu, C. Randorn, P. Efstathiou, J.T.S. Irvine, Nat. Mater. 11 (2012) 595–598.
[4] X.Q. Sun, Y.L. Mi, F. Jiao, X.X. Xu, ACS Catal. 8 (2018) 3209–3221.
[5] S.H. Wei, X.X. Xu, Appl. Catal. B-Environ. 228 (2018) 10–18.
[6] L.W. Lu, M.L. Lv, D. Wang, G. Liu, X.X. Xu, Appl. Catal. B-Environ. 200 (2017) 412–419.
[7] M.L. Lv, G. Liu, X.X. Xu, ACS Appl. Mater. Inter. 8 (2016) 28700–28708.
[8] M.L. Lv, S. Ni, Z. Wang, T.C. Cao, X.X. Xu, Int. J. Hydrogen Energ. 41 (2016) 1550–1558.
[9] M.L. Lv, Y.W. Wang, L.W. Lu, R.N. Wang, S. Ni, G. Liu, X.X. Xu, Phys. Chem. Chem. Phys. 18 (2016) 21491–21499.
[10] M.L. Lv, Y.H. Xie, Y.W. Wang, X.Q. Sun, F.F. Wu, H.M. Chen, S.W. Wang, C. Shen, Z.F. Chen, S. Ni, G. Liu, X.X. Xu, Phys. Chem. Chem. Phys. 17 (2015) 26320–26329.
[11] X.Q. Sun, G. Liu, X.X. Xu, J. Mater. Chem. A Mater. Energy Sustain. 6 (2018) 10947–10957.
[12] X.Q. Sun, S.W. Wang, C. Shen, X.X. Xu, ChemCatChem 8 (2016) 2289–2295.
[13] X.Q. Sun, Y.H. Xie, F.F. Wu, H.M. Chen, M.L. Lv, S. Ni, G. Liu, X.X. Xu, Inorg. Chem.

54 (2015) 7445–7453.

[14] X.Q. Sun, X.X. Xu, Appl. Catal. B-Environ. 210 (2017) 149–159.

[15] S.Y. Reece, J.A. Hamel, K. Sung, T.D. Jarvi, A.J. Esswein, J.J.H. Pijpers, D.G. Nocera, Science 334 (2011) 645–648.

[16] H. Zhang, S. Ni, Y.L. Mi, X.X. Xu, J. Catal. 359 (2018) 112–121.

[17] J.A. Turner, Science 305 (2004) 972–974.

[18] F.X. Wan, C.H. Wang, Y.H. Han, L. Kong, J.Y. Yan, X.T. Zhang, Y.C. Liu, Dalton Trans. 47 (2018) 13608–13615.

[19] H. Zheng, C.H. Wang, X.T. Zhang, Y.Y. Li, H. Ma, Y.C. Liu, Appl. Catal. B-Environ. 234 (2018) 79–89.

[20] C.H. Wang, X.T. Zhang, Y.C. Liu, Appl. Surf. Sci. 358 (2015) 28–45.

[21] Y.H. Xie, Y.W. Wang, Z.F. Chen, X.X. Xu, Chemsuschem 9 (2016) 1403–1412.

[22] Y.W. Wang, D.Z. Zhu, X.X. Xu, ACS Appl. Mater. Inter. 8 (2016) 35407–35418.

[23] S.H. Wei, G. Zhang, X.X. Xu, Appl. Catal. B-Environ. 237 (2018) 373–381.

[24] F.F. Wu, X.Q. Sun, G. Liu, X.X. Xu, Catal. Sci. Technol. 7 (2017) 4640–4647.

[25] F.F. Wu, M.L. Lv, X.Q. Sun, Y.H. Xie, H.M. Chen, S. Ni, G. Liu, X.X. Xu, ChemCatChem 8 (2016) 615–623.

[26] M.R. Hoffmann, S.T. Martin, W.Y. Choi, D.W. Bahnemann, Chem. Rev. 95 (1995) 69–96.

[27] R.N. Wang, S. Ni, G. Liu, X.X. Xu, Appl. Catal. B-Environ. 225 (2018) 139–147.

[28] J.R. Ran, M. Jaroniec, S.Z. Qiao, Adv. Mater. 30 (2018).

[29] M.S. Zhu, S. Kim, L. Mao, M. Fujitsuka, J.Y. Zhang, X.C. Wang, T. Majima, J. Am. Chem. Soc. 139 (2017) 13234–13242.

[30] S. Ida, A. Takashiba, S. Koga, H. Hagiwara, T. Ishihara, J. Am. Chem. Soc. 136 (2014) 1872–1878.

[31] K. Zhang, W. Kim, M. Ma, X. Shi, J.H. Park, J. Mater. Chem. A Mater. Energy Sustain. 3 (2015) 4803–4810.

[32] J. Zhang, S.Z. Qiao, L.F. Qi, J.G. Yu, Phys. Chem. Chem. Phys. 15 (2013) 12088–12094.

[33] J. Zhang, Z.P. Zhu, X.L. Feng, Chem.-Eur. J. 20 (2014) 10632–10635.

[34] S. Iqbal, Z.W. Pan, K.B. Zhou, Nanoscale 9 (2017) 6638–6642.

[35] B. Wang, S.X. Yang, C. Wang, M.H. Wu, L. Huang, Q. Liu, C.B. Jiang, Nanoscale 9 (2017) 10733–10740.

[36] M.G. Wang, Y.M. Hu, J. Han, R. Guo, H.X. Xiong, Y.D. Yin, J. Mater. Chem. A Mater. Energy Sustain. 3 (2015) 20727–20735.

[37] L. Pan, S.B. Wang, J.W. Xie, L. Wang, X.W. Zhang, J.J. Zou, Nano Energy 28 (2016)

296–303.

[38] L.J. Wang, W.Z. Wang, Y.L. Chen, L.Z. Yao, X. Zhao, H.L. Shi, M.S. Cao, Y.J. Liang, ACS Appl. Mater. Inter. 10 (2018) 11652–11662.

[39] Y. Zhao, X. Huang, X. Tan, T. Yu, X.L. Li, L.B. Yang, S.C. Wang, Appl. Surf. Sci. 365 (2016) 209–217.

[40] L. Wang, X.S. Zheng, L. Chen, Y.J. Xiong, H.X. Xu, Angew. Chemie Int. Ed. English 57 (2018) 3454–3458.

[41] M.S. Zhu, X.Y. Cai, M. Fujitsuka, J.Y. Zhang, T. Majima, Angew. Chemie Int. Ed. English 56 (2017) 2064–2068.

[42] Z.B. Fang, X.Y. Huang, Y.Z. Wang, W.H. Feng, Y. Zhang, S.X. Weng, X.Z. Fu, P. Liu, J. Mater. Chem. A Mater. Energy Sustain. 4 (2016) 13980–13988.

[43] X.X. Xu, G. Liu, C. Randorn, J.T.S. Irvine, Int. J. Hydrogen Energ. 36 (2011) 13501–13507.

[44] W.J. Huang, L. Gan, H.T. Yang, N. Zhou, R.Y. Wang, W.H. Wu, H.Q. Li, Y. Ma, H.B. Zeng, T.Y. Zhai, Adv. Funct. Mater. 27 (2017).

[45] X.Y. Cai, J.Y. Zhang, M. Fujitsuka, T. Majima, Appl. Catal. B-Environ. 202 (2017) 191–198.

[46] E.B. Hua, G. Liu, G. Zhang, X.X. Xu, Dalton Trans. 47 (2018) 4360–4367.

[47] M.L. Lv, X.Q. Sun, S.H. Wei, C. Shen, Y.L. Mi, X.X. Xu, ACS Nano 11 (2017) 11441–11448.

[48] H.M. Chen, Y.H. Xie, X.Q. Sun, M.L. Lv, F.F. Wu, L. Zhang, L. Li, X.X. Xu, Dalton Trans. 44 (2015) 13030–13039.

[49] S. Thaweesak, M.Q. Lyu, P. Peerakiatkhajohn, T. Butburee, B. Luo, H.J. Chen, L.Z. Wang, Appl. Catal. B-Environ. 202 (2017) 184–190.

[50] C. Chen, Z.P. Gao, H.X. Yan, M.J. Reece, J. Am. Ceram. Soc. 99 (2016) 523–530.

[51] A. Orera, G. Larraz, M.L. Sanjuan, J. Eur. Ceram. Soc. 33 (2013) 2103–2110.

[52] W.Z. Weng, H.L. Wan, J.M. Li, Z.X. Cao, Angew. Chemie Int. Ed. English 43 (2004) 975–977.

[53] C.E. Housecroft, A.G. Sharpe, Inorganic Chemistry, third edition, Pearson Education Limited, England, 2008.

[54] M. Dan, Q. Zhang, S. Yu, A. Prakash, Y.H. Lin, Y. Zhou, Appl. Catal. B-Environ. 217 (2017) 530–539.

[55] Q.R. Zhang, M.B. Luo, Y.P. Sun, Y.F. Liu, A.N. Cao, Nanotechnology 27 (2016).

[56] S.J. Hu, B. Chi, J. Pu, L. Jian, J. Mater. Chem. A Mater. Energy Sustain. 2 (2014) 19260–19267.